Conformational disorder in energy transfer: beyond Förster theory†

Tammie Nelson,[a] Sebastian Fernandez-Alberti,[b] Adrian E. Roitberg[c] and Sergei Tretiak*[a]

Energy transfer in donor–acceptor chromophore pairs, where the absorption of each species is well separated while donor emission and acceptor absorption overlap, can be understood through a Förster resonance energy transfer model. The picture is more complex for organic conjugated polymers, where the total absorption spectrum can be described as a sum of the individual contributions from each subunit (chromophore), whose absorption is not well separated. Although excitations in these systems tend to be well localized, traditional *donors* and *acceptors* cannot be defined and energy transfer can occur through various pathways where each subunit (chromophore) is capable of playing either role. In addition, fast torsional motions between individual monomers can break conjugation and lead to reordering of excited state energy levels. Fast torsional fluctuations occur on the same timescale as electronic transitions leading to multiple trivial unavoided crossings between excited states during dynamics. We use the non-adiabatic excited state molecular dynamics (NA-ESMD) approach to simulate energy transfer between two poly-phenylene vinylene (PPV) oligomers composed of 3-rings and 4-rings, respectively, separated by varying distances. The change in the spatial localization of the transient electronic transition density, initially localized on the donors, is used to determine the transfer rate. Our analysis shows that evolution of the intramolecular transition density can be decomposed into contributions from multiple transfer pathways. Here we present a detailed analysis of ensemble dynamics as well as a few representative trajectories which demonstrate the intertwined role of electronic and conformational processes. Our study reveals the complex nature of energy transfer in organic conjugated polymer systems and emphasizes the caution that must be taken in performing such an analysis when a single simple unidirectional pathway is unlikely.

I. Introduction

In recent years, organic conjugated polymers have become popular materials for use in photovoltaic applications,[1–3] and have shown excellent light harvesting and sensitizing properties.[4–7] The highly polarizable and delocalized π-electrons of organic conjugated molecules are responsible for many of the unique electronic and photophysical properties associated with these materials.[8,9] Following light absorption, the photoinduced electronic excitation undergoes energy transfer (ET) to lower energy sites where emission or charge separation occurs.[10–12] Developing a clear picture of the complex photoexcitation dynamics in such materials is essential to providing an accurate description of the underlying photophysical processes such as exciton formation, evolution, and decay *via* non-adiabatic (NA) dynamics.[13,14]

Förster resonance energy transfer (FRET) is typically used to describe energy transfer between donor and acceptor chromophores.[15] In FRET, an excited donor fluorophore can transfer excited state energy to a nearby acceptor. Förster theory is based on a point dipole approximation, namely that the distance between the moieties is much larger than the size of the individual donor or acceptor dipoles.[16–18] The efficiency of energy transfer depends on the distance between donor and acceptor, their spectral characteristics, and their relative orientation.[19–23] In order for transfer to be efficient, the donor and acceptor absorption must be well separated, while the donor emission spectrum must overlap with the absorption of the acceptor.[24–27]

[a] *Theoretical Division, Center for Nonlinear Studies (CNLS), and Center for Integrated Nanotechnologies (CINT), Los Alamos National Laboratory, Los Alamos, New Mexico 87545, USA. E-mail: serg@lanl.gov, tretiak@lanl.gov*
[b] *Universidad Nacional de Quilmes, Roque Saenz Pea 352, B1876BXD Bernal, Argentina*
[c] *Departments of Physics and Chemistry, Quantum Theory Project, University of Florida, Gainesville, FL 32611, USA*
† Electronic supplementary information (ESI) available. See DOI: 10.1039/c3cp50857a

This journal is © the Owner Societies 2013

Phys. Chem. Chem. Phys., 2013, **15**, 9245–9256 | **9245**

In conjugated organic polymers, such as poly-phenylene vinylene (PPV) linear segments of varying lengths can act as weakly coupled chromophore units. Therefore, the total absorption spectrum can be interpreted as the sum of the contributions from each fragment with strong overlap between the component absorption spectra.[28,29] Fragments of varying length localize excitons and create an intramolecular energy gradient. Following photoexcitation, energy is transferred non-radiatively between the segments.[10,30,31] Unlike traditional FRET where the isolated absorption of the donor allows for selective excitation, the overlapping absorption of the fragments in these systems means that either fragment can act as the *donor* or *acceptor* depending on where the initial excitation is localized. This unique feature of conjugated organic polymers gives rise to a much richer energy transfer dynamics involving various pathways which must be considered.

Large inter-ring dihedral angles between the monomer subunits can break the conjugation producing electronically coupled conformational subfragments and leading to reordering of the excited state energy levels.[30,32–34] In general, upon photoexcitation, the molecular conformation relaxes towards a new equilibrium geometry typically on a tens of picoseconds timescale. However, it has recently been demonstrated that in oligofluorenes in solution, the torsional relaxation can be sped up from 10 ps to <0.1 ps depending on which state is excited.[35] For the specific case of breaking or restoring conjugation, complete torsional relaxation or planarization is not required. Instead small fluctuations in the dihedral angle around certain particularly distorted instantaneous molecular configurations can lead to changes in exciton localization. When these relatively fast fluctuations occur on the same timescale as electronic relaxation, the interplay between conformation and energy transfer dynamics must be addressed.

Conformational defects are typically treated as either static or dynamic. Static defects involve large torsion angles between subunits that act as conjugation breaks and are assumed to evolve slowly in time compared to excitation motion. On the other hand, the dynamic defects can undergo complete conformational relaxation before energy transfer or so-called "hot energy transfer" from the unrelaxed, twisted, conformation.[32] However, conformational *fluctuations* must be included in real molecules. Fluctuations in the torsion angles/bond lengths and electronic relaxation may occur simultaneously. Thus, energy transfer occurs between 'dynamical' rather than 'static' polymers whose torsional motions along the backbone of each segment cause energy reordering of excited states or quasi-degeneracy resulting in ultrafast changes to exciton localization. At the same time, electronic relaxation takes place between excited states whose character and localization is constantly changing.

It is well known that among the PPV family, and other conjugated polymers, neighboring conformational subfragments formed by conjugation breaks can electronically couple to one another forming delocalized collective states that influence optical properties.[31,36] In systems with multiple chromophores, such as natural light harvesting complexes, energy transfer involves excitons delocalized over multiple chromophores; As long as the donor and acceptor sites are well separated, a rate description based on the Förster theory can still be applied.[37] Multichromophoric Förster resonance energy transfer (MC-FRET) theories have been developed over the years[38–42] to treat systems where application of single chromophore descriptions can lead to significant errors due to the breakdown of the point-dipole approximation and because more than one pair of excitations is involved in the transfer. However, even sophisticated MC-FRET theories can only treat static energy disorder,[40] and the distance dependence can vary with disorder and temperature.[38]

Torsional dynamics along the conjugated backbone can have a pronounced effect on energy transfer. The presence of conformational disorder in conjugated polymers[30,43–46] induces spatial confinement of electronic excitations and affects the molecular relaxation pathways. These conformational subunits act as primary absorbing units. After excitation of a subunit, energy is funneled to lower-energy sites either on the same chain or on another chain by energy transfer. Experimental evidence for this energy transfer can be seen in the measurement of polarization anisotropy decays in samples of MEH-PPV.[31,36,47,48] These experiments reveal that energy migration occurs over timescales ranging from a few to hundreds of picoseconds.[31] In 2003, Grage *et al.*[47] measured the energy migration between MEH-PPV conformational subunits formed by replacing a portion of vinylene double bonds with single bonds to act as conjugation breaks and found an average hopping time of 0.3 ps between adjacent chromophore units. They also confirmed that polymers with fewer conjugation breaks are stiffer, have less conformational disorder, and are characterized by higher anisotropy and slower hopping times. Thus, the degree of conformational disorder strongly influences the available energy transfer pathways. We expect that PPV should exhibit properties similar to those observed in partially deconjugated MEH-PPV with many short chromophore units (2–3 monomers) and large conformational disorder, on which the energy transfer between configurational subunits located on the same oligomer fragment will be very efficient due to short distances and good spectral overlap.

Here, we use the non-adiabatic excited state molecular dynamics (NA-ESMD) framework[49] to investigate energy transfer between two poly-phenylene vinylene (PPV) segments composed of 3-rings and 4-rings separated by varying distances. We compare our results to Förster theory used to model the energy transfer between weakly coupled molecular electronic transition dipoles and demonstrate that the popular model does not work well for these systems due to the multiple photoinduced pathways involved, including 3- to 4-rings and 4- to 3-rings, and the sudden changes in excitation localization caused by torsional fluctuations. The specific energy transfer pathway depends on the initial excitation localization which is governed by both the configuration and the initial electronic state. The conformational fluctuations lead to reordering of excited state energies and result in trivial unavoided crossings of the adiabatic potential energy surfaces. Failure to detect these crossings can lead to the sudden unrealistic transfer of the electronic transition density localization of the current state from one segment to another, leading to false results. To avoid this problem, we use the

previously developed method to detect trivial unavoided crossings during non-adiabatic dynamics by tracking the identities of individual excited states.[50] While FRET involves eventual fluorescence emission from the lowest energy excited state for the donor, here we consider only non-radiative energy transfer where the final state of the system is the lowest energy S_1 excited state.

Section II provides a brief description of the NA-ESMD theoretical approach and discusses transition density calculations and an overview of Förster theory. In Section III, our simulation results are presented including analysis of transition density decay, energy reordering of excited states due to dihedral angles, and an in depth analysis of the interaction between excitation localization and configurational fluctuations for a few representative trajectories. Our findings are summarized in Section IV.

II. Theoretical methodology

A. The NA-ESMD background

The NA-ESMD simulations combine the molecular dynamics with quantum transitions (MDQT) approach with "on the fly" analytical calculations of excited state energies,[51] gradients,[52] and non-adiabatic coupling terms[49,53] in order to describe the photoinduced dynamics in large conjugated organic molecules involving many coupled electronic excited states. Correlated excited states are described in the NA-ESMD framework using the collective electronic oscillator (CEO) method[54,55] applied at the Austin Model 1 (AM1)[56] level of theory in combination with a configuration interaction singles (CIS) formalism.

MDQT treats the electronic degrees of freedom quantum mechanically, while the motion of the nuclei is treated classically. Our simulations propagate a swarm of independent classical trajectories evolving along the excited state manifold. The initial geometries are sampled from a thermally equilibrated ground state trajectory. The statistical average over these independent trajectories constitutes a photoexcited electronic wavepacket. Initially the width of this wavepacket reflects the initial configurational disorder of the ensemble. At any given time, the nuclei of each trajectory are evolved on a single adiabatic potential energy surface (PES) rather than in the mean field, and transitions between coupled electronic states are possible depending on the strength of the non-adiabatic coupling.[57] Specifically, the Fewest Switches Surface Hopping[58,59] (FSSH) algorithm is used. The nuclei are propagated using the Velocity Verlet algorithm[60] combined with a constant-temperature Langevin dynamics algorithm[61] developed to be consistent with the velocity Verlet integration technique.[62] Details of NA-ESMD implementation and limitations can be found in our previous work.[49,63] Although solvent is not explicitly included in our simulations, a phenomenological description of solvent effects in included by using the Langevin equation of motion which incorporates frictional damping and a fluctuating force following the fluctuation-dissipation theorem.[61]

During photoinduced dynamics in extended conjugated molecules, trivial unavoided crossings between non-interacting states can take place. During the NA-ESMD simulations, nuclear motion through such crossings should result in the system remaining on the same diabatic state. Because of that, the identity of the electronic states at each time during dynamics cannot be followed based on the energy-ordering criterion. In addition, trivial unavoided crossings are characterized by nonadiabatic couplings described as sharp peaks strongly localized at the exact crossing points. More precisely, while becoming nearly infinite at the exact crossing point, nonadiabatic couplings vanish elsewhere. This feature, in combination with the use of finite time-step numerical propagators for the classical nuclear motion, can cause trivial unavoided crossings to be missed. This failure can lead to unphysical sudden changes in the spatial localization of the transition density of the current state. Neglecting to treat the unavoided crossings will result in artifical long-distance energy transfer. In order to avoid this problem it is necessary to track the identities of the states over time. New states at the current time step i are assigned in terms of old states at the preceding time step ($i - 1$) according to a state reassignment procedure described in detail elsewhere.[50]

B. Molecular dynamics simulations

Model systems depicted in Fig. 1 are composed of 3- and 4-ring PPV segments. For small separation distances, the segments are linked by an alkyl chain whose length is varied. The separation distance, r_{CM}, is defined as the distance between the centers of mass of each segment. For each of the linked systems, a ground state molecular dynamics trajectory was performed for 650 ps with a friction coefficient of 2.0 ps^{-1} (an optimum parameter for Langevin dynamics simulations in water[62,63]) at 300 K starting from an AM1 optimized structure. Snapshots were collected at 500 fs intervals to provide the initial positions and momenta for subsequent excited state simulations. In all of the selected snapshots, the 3- and 4-ring segments are in the *cis*-conformation with respect to one another, as shown in Fig. 1. Next, in order to create larger separation distances, we start with the snapshots collected
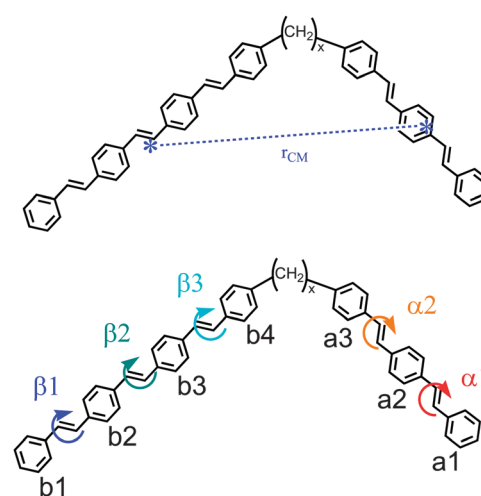

Fig. 1 Top: Chemical structure of the PPV oligomers studied in this work. A 3-ring segment and a 4-ring segment are joined by an alkyl chain of length *x*. The separation distance, r_{CM}, is measured as the distance between the centers of mass of the two segments. For larger separation distances, the alkyl chain is removed. Bottom: labeling scheme for dihedral twist angles and subunits.

from the $x = 1$ ground state trajectory and remove the alkyl chain. A terminal hydrogen atom was placed at the end of each segment, and the segments were separated to the desired distance by increasing r_{CM} along the center of mass vector. Furthermore, the resulting unlinked geometries were relaxed by performing molecular dynamics in the ground state for an additional 50 fs.

The PPV fragments act as weakly coupled chromophore units allowing the total absorption spectrum to be interpreted as the sum of the contributions from each segment as shown in the bottom panel of Fig. 2. The initial excited state was chosen according to a Frank–Condon window defined as

$$g_\alpha(r, \boldsymbol{R}) = \exp[-T^2(E_{laser} - \Omega_\alpha)^2], \qquad (1)$$

where E_{laser} represents the energy of a laser centered at $\lambda_{laser} = 370$ nm, and Ω_α represents the energy of state α (expressed in units of fs^{-1}) from the theoretical absorption spectrum. The laser shape is assumed to be Gaussian $f(t) = \exp(-t^2/2T^2)$, $T^2 = 42.5$ fs corresponding to a FWHM of 100 fs. The initial excitation is selected according to the relative values of $g_\alpha(r, \boldsymbol{R})$ weighted by
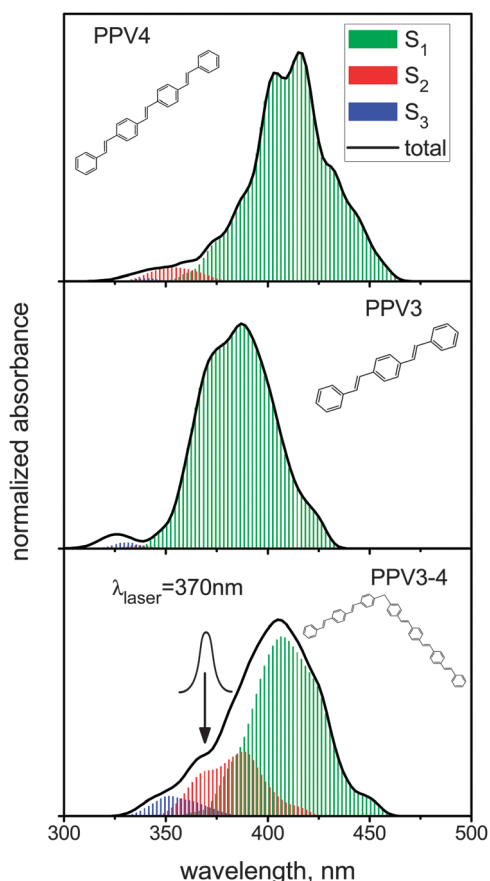

Fig. 2 Calculated absorption spectra of the isolated 4-ring (top) and 3-ring (middle) PPV oligomers. Bottom: The spectrum for the combined system ($x = 1$) can be interpreted as a sum of the contributions from each fragment. The S_1 state is contributed by the 4-ring segment and the S_2 state is derived from the 3-ring segment. A Frank–Condon window defined by a Gaussian shaped laser centered at $\lambda_{laser} = 370$ nm with FWHM of 100 fs was used to populate the initial excited states.

the oscillator strengths of each state α where the 5 lowest energy excited states have been considered. A swarm of 1080 NA-ESMD trajectories was propagated for 1 ps at 300 K where 5 electronic excited states and their non-adiabatic coupling vectors have been included in the simulations. The nuclei were propagated with a classical time step of $\Delta t = 0.1$ fs, with $N_q = 10$ quantum time steps per classical step for the evaluation of the non-adiabatic couplings and propagation of the quantum coefficients. The quantum time step was further reduced by a factor of 40 for the detection of possible trivial unavoided crossings.[50]

C. Transition density localization

The transition density matrices are defined as[52,54,64]

$$(\rho^{ga})_{nm} = \langle \phi_\alpha(r; \boldsymbol{R}(t)) \times |c_m^+ c_n| \phi_g(r; \boldsymbol{R}(t)) \rangle \qquad (2)$$

where $\phi_g(r; \boldsymbol{R}(t))$ is the Hartree–Fock ground state (GS) and $\phi_\alpha(r; \boldsymbol{R}(t))$ are the CIS adiabatic excited state wavefunctions, respectively. c_m^+ and c_n represent the creation and annihilation operators, and n and m indices refer to the atomic orbital (AO) basis functions. The diagonal elements $(\rho^{ga})_{nn}$ represent the net change in the distribution of the electronic density induced by an optical excitation from the ground state g to an excited electronic state α. The usual normalization condition $\sum_{n,m} (\rho^{ga})_{nm}^2 = 1$ holds for the CIS approximation.[51,65] Therefore, the fraction of the transition density localized on each PPV segment (3-ring and 4-ring segments) is obtained by summing the contributions from each atom belonging to the segment as follows

$$(\rho^{ga})_{X\text{-ring}}^2 = \sum_{n_A m_A} (\rho^{ga})_{n_A m_A}^2 + \frac{1}{2} \sum_{n_B m_B} (\rho^{ga})_{n_B m_B}^2 \qquad (3)$$

where $X = 3, 4$. The index A runs over all atoms localized in the segment of interest and the index B runs over atoms localized on the linking alkyl chain (if present). Consequently, in our case $\sum_X (\rho^{ga})_{X\text{-ring}}^2 \approx 1$, given that there are no charge-transfer excitations between molecular fragments.

In order to calculate the rate for the energy transfer process, the time evolution of the transition density averaged over the swarm of NA-ESMD trajectories is fit to a biexponential decay function of the form $f(t) = A \exp(-t/\tau_1) + (B - A)\exp(-t/\tau_2)$ where τ_1 and τ_2 represent the slow and fast decay timescales, respectively, and B is the initial transition density at time $t = 0$. The overall rate is related to the timescale as $k_{DA} = \frac{1}{\Gamma}$ where Γ is the weighted sum of the slow and fast timescales $\Gamma = A\tau_1 + (B - A)\tau_2$.

D. Förster energy transfer

The dipole–dipole interaction, V, between molecular electronic transition dipole moments of a weakly coupled donor (D) and acceptor (A) is given by

$$V_{DA} = \frac{3(\bar{\mu}_A \hat{r})(\bar{\mu}_D \hat{r}) - \bar{\mu}_A \bar{\mu}_D}{r^3} \qquad (4)$$

where $\bar{\mu}_{D(A)}$ is the transition dipole moment that couples the ground and excited electronic states of the donor(acceptor), r is the distance between the centers of the dipoles, and $\hat{r}$ is the

vector connecting them. The expression in eqn (4) is valid for the so-called independent dipole approximation or point dipole approximation,[16,18,66] where the distance r is much larger than either dipole. Variations in the dipole description, such as distributed monopoles or the line-dipole approximation can be used to account for the failure of the point-dipole approximation in Förster theory.[67] The line-dipole approximation involves distributing the transition dipole moments over individual subunits and summing over their pairwise interactions.[68]

The electronic transition dipole interaction can also be written as[19,27]

$$V_{DA} = \frac{\bar{\mu}_A \bar{\mu}_D}{r^3}(\cos\alpha - 3\cos\beta_1\cos\beta_2) \qquad (5)$$

where α is the angle between the dipoles, and β_1 and β_2 are the angles between each dipole and the vector $\hat{r}$ connecting them. The transition rate, k_{DA}, can be expressed using Fermi's Golden rule

$$k_{DA} = \frac{2\pi}{\hbar^2}|V_{DA}|^2 J_{DA} \qquad (6)$$

where J_{DA} is the spectral overlap between donor emission and acceptor absorption. The rate of energy transfer according to Förster theory scales as r^{-6} (ref. 15, 19 and 21)

$$k_{DA} = \frac{1}{\tau_D}\left(\frac{R_0}{r^6}\right). \qquad (7)$$

Here τ_D represents the fluorescence lifetime of the donor in the absence of the acceptor, and R_0 is the so-called critical transfer distance, that is the distance at which the probability of transfer is 50%.

III. Results

The NA-ESMD simulations have been performed in order to investigate the energy transfer between PPV segments of the model molecule depicted in Fig. 1. The separation distances, r_{CM}, for the ground-state AM1 optimized structures are provided in Table 1. A Frank–Condon window defined by a Gaussian shaped laser centered at λ_{laser} = 370 nm with FWHM of 100 fs was used to populate the initial excited states according to their contributions to the simulated absorption spectrum shown in Fig. 2. The absorbance spectra of the isolated 4-ring and 3-ring PPV segments are shown in the first two panels, respectively. The contributions of the different excited states to the absorption spectrum for the combined system (x = 1) are shown in the bottom panel. The peak at 410 nm for the combined system corresponds to the S_1 state whose absorbance coincides with the absorption maximum for the isolated 4-ring segment indicating that its contribution comes from the 4-ring segment. Similarly, the peak at 390 nm for the combined system corresponds to the S_2 state and its absorbance coincides with the absorption maximum for the isolated 3-ring segment indicating that the S_2 state is derived from the 3-ring segment. Thus, for the equilibrium geometry, we expect the lowest energy S_1 excited state to be localized on the 4-ring segment while S_2 is localized on the 3-ring segment.

Table 1 Separation distances between the centers of mass of the 3- and 4-ring segments for the GS optimized systems

x	r_{CM} (Å)
x = 1	19.5
x = 5	24.5
x = 11	31.1
—	50
—	100
—	200
—	500

The initial localization of the transition density is shown in Fig. 3A for the AM1 optimized planar ground-state geometry. The lowest energy excited state, $S_1^{(4)}$, is localized on the 4-ring segment. In our notation, the subscript indicates the usual energy ordering of the state and the superscript indicates the segment where the excitation is localized. The second state, $S_2^{(3)}$, has transition density localized on the 3-ring fragment while the third state is localized on the 4-ring side, $S_3^{(4)}$. Excitation at 370 nm allows us to preferentially select absorption by S_2 and minimize absorption by the overlapping S_3 state. Consider one possible scenario depicted in Fig. 3B: following photoexcitation to $S_2^{(3)}$ the initial transition density localized on the 3-ring segment is transferred to the 4-ring segment as the system undergoes non-radiative relaxation to $S_1^{(4)}$, and the process has an associated timescale, Γ. Since the initial transition density localization depends on both the initial state and the initial configuration, we can also imagine the scenario shown in Fig. 3C. Here, the visibly twisted configuration causes reordering of the excited state energies and the second excited state becomes localized on the 4-ring segment, $S_2^{(4)}$, while the lowest state is now localized on the 3-ring segment, $S_1^{(3)}$, and the transfer proceeds in the "reverse" direction.

A. Intramolecular redistribution of initial transition density

The presence of multiple crossings between adiabatic states means that electronic excited states cannot be identified based simply on their energy ordering and therefore the adiabatic
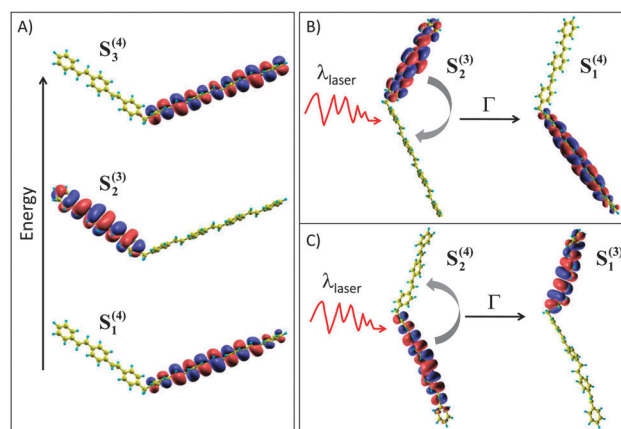

Fig. 3 (A) Initial transition density localization for the three lowest energy excited electronic states. Following photoexcitation at 370 nm energy transfer can proceed through multiple pathways (B) 3-ring → 4-ring and (C) 4-ring → 3-ring made possible by different conformations.

electronic state populations can no longer be used as an accurate measure of energy transfer. Instead, energy transfer can be revealed by following the time-evolution of the spatial localization of the electronic transition density for the current state.[50] The decay of the fraction of the transition density localized on the 3-ring segment is shown in Fig. 4. Here, we have averaged over all NA-ESMD trajectories, where N_{tot} is the number of trajectories, and therefore refer to this as the total transition density $\langle (\rho^{ga})_{3\text{-ring}}{}^2 \rangle_{N_{tot}}$. According to the decay of the total transition densities, the rate of energy transfer from the 3-ring segment tends to decrease as the separation distance increases, as expected.

However, the total transition density does not reflect the multiple distinct pathways for energy transfer, that is 3-rings → 4-rings or the reverse 4-rings → 3-rings. Multiple pathways exist for two reasons: first, our laser pulse has an associated width meaning that we cannot exclude the possibility that S_3 has been selected as the initial excitation. Second, the initial conformational sampling contains dihedral rotations that break the full conjugation and can cause a reordering of excited state energies. Therefore, S_2 can be localized on either the 3-ring or 4-ring side, $S_2^{(3)}$ and $S_2^{(4)}$, respectively. Similarly, S_3 can be localized on either segment as well, $S_3^{(3)}$ or $S_3^{(4)}$.

We continue our analysis by dividing the total transition density decay into different contributions depending on the initial transition density localization and initial state as shown schematically in Fig. 5. Specifically we divide the NA-ESMD trajectories into two groups: (i) those whose initial transition density is localized on the 4-ring segment where $(\rho^{ga})_{4\text{-ring}}{}^2 > 80\%$ and (ii) those whose initial transition density is localized on the 3-ring segment where $(\rho^{ga})_{3\text{-ring}}{}^2 > 80\%$. The quantities $\left\langle (\rho^{ga})_{4\text{-ring}}{}^2 \right\rangle_{N_{S^{(4)}}}$ and $\left\langle (\rho^{ga})_{3\text{-ring}}{}^2 \right\rangle_{N_{S^{(3)}}}$ represent the transition densities averaged over the swarm of trajectories from groups (i) and (ii), respectively, where $N_{S^{(4)}}$ is the number of trajectories in group (i) and $N_{S^{(3)}}$ is the number of trajectories in group (ii).
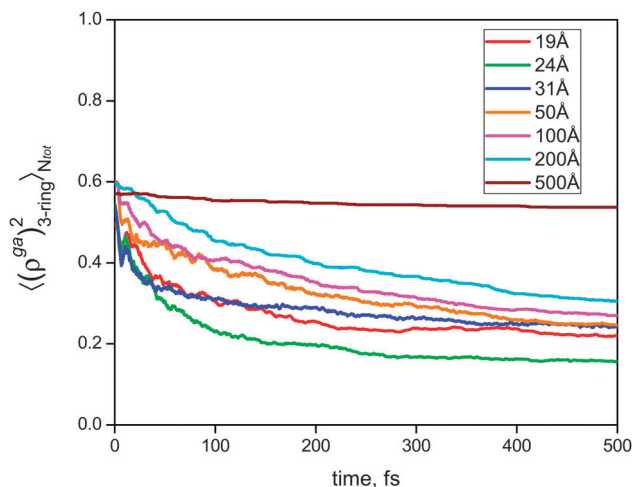

Fig. 4 Energy transfer is revealed through the decay of the electronic transition density. Here the transition density localized on the 3-ring segment averaged over all NA-ESMD trajectories, N_{tot}, is plotted for the varying separation distances.
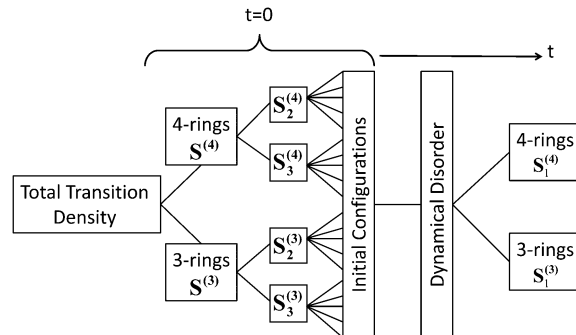

Fig. 5 The total transition density comprised of all trajectories can be divided into contributions according to the initial localization of the electronic transition density (4-rings or 3-rings) which is influenced by the initial state and by the configuration. Dynamical disorder causes the configuration to change in time, such that the final state at some later time t may be localized on either segment.

The data in Table 2 shows the number of trajectories in each group (i) and (ii) as well as the number of trajectories starting in a mixed state, that is where the transition density is not localized on either segment. As the separation distance increases, the relative number of mixed state configurations decreases as the coupling becomes weaker. The mixed state configurations are not considered in the our analysis, since we do not have enough statistics to analyze these cases.

First, we consider separately the decay of the average transition density localized on the 4-ring segment for group (i) and the 3-ring segment for group (ii) shown in the top and bottom panels of Fig. 6, respectively. Trajectories that start on the 4-ring segment do not undergo complete energy transfer, as can be seen by the fact that the transition density localized on the 4-ring segment never falls below 65%. At short times, density is transferred from the 4-ring segment to the 3-ring segment. As the dynamics continues, the density on the 4-ring segment begins to rise. This is a consequence of the 3-state problem: if we assume that of the three lowest energy excited states, two are localized on the 4-ring side and one is localized on the 3-ring side, then depending on the initial state ($S_2^{(4)}$ or $S_3^{(4)}$) there are four possible pathways $S_2^{(4)} \rightarrow S_1^{(4)}$, $S_2^{(4)} \rightarrow S_1^{(3)}$, $S_3^{(4)} \rightarrow S_2^{(3)} \rightarrow S_1^{(4)}$, or $S_3^{(4)} \rightarrow S_2^{(3)} \rightarrow S_1^{(4)}$ where energy transfer might or might not occur. The first 3 pathways can be mapped onto a two-state model, while the 4th pathway is a three-state

Table 2 Number of trajectories (and relative percentages) for each of the groups: total (N_{tot}), initial localization on 4-rings ($N_{S^{(4)}}$) or 3-rings ($N_{S^{(3)}}$), mixed states (N_{mix}), initially promoted to S_2 localized on 3-rings $\left(N_{S_2^{(3)}} \right)$ and initially promoted to S_3 localized on 3-rings $\left(N_{S_3^{(3)}} \right)$

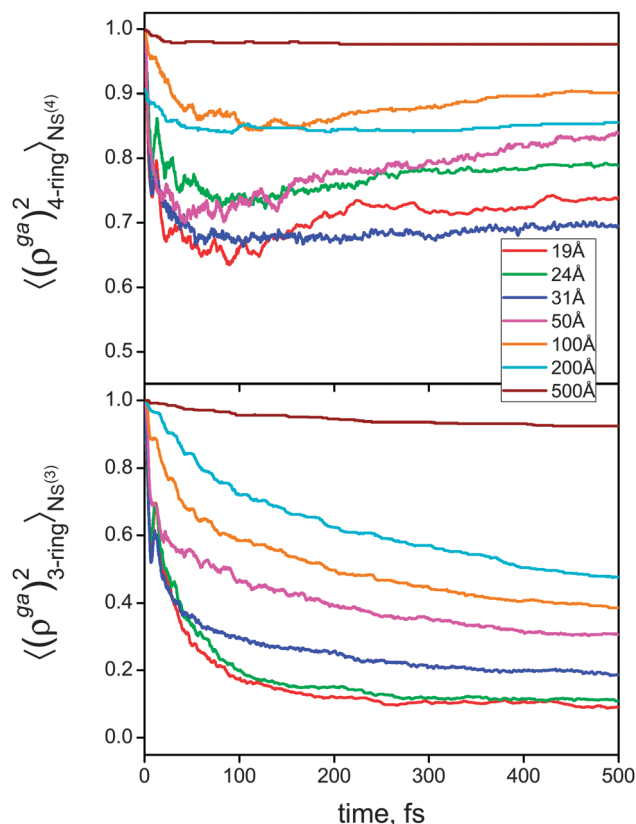| r_{CM} (Å)	N_{tot} (%)	N_{mix} (%)	$N_{S^{(4)}}$ (%)	$N_{S^{(3)}}$ (%)	$N_{S_2^{(3)}}$ (%)	$N_{S_3^{(3)}}$ (%)
19	1021	208 (20.4)	452 (44.3)	361 (35.3)	340 (33.3)	21 (2.0)
24	976	71 (7.3)	400 (41.0)	505 (51.7)	470 (48.1)	35 (3.6)
31	1020	23 (2.3)	451 (44.2)	546 (53.5)	511 (50.1)	35 (3.4)
50	1077	12 (1.1)	425 (39.5)	640 (59.4)	594 (55.1)	46 (4.3)
100	1074	7 (0.7)	428 (39.8)	639 (59.5)	596 (55.5)	43 (4.0)
200	1077	6 (0.6)	432 (40.1)	639 (59.3)	598 (55.5)	41 (3.8)
500	1075	5 (0.5)	458 (42.6)	612 (56.9)	593 (55.2)	19 (1.7)

Fig. 6 The total transition density is divided into contributions from trajectories (top) initially localized on the 4-ring segment and (bottom) those initially localized on the 3-ring segment. The change in the electronic transition density with time is plotted for each separation distance.

process. Here the density is first transferred to the 3-ring segment, at later times the competing transfer to the lower energy state localized on the 4-ring segment enters the process leading to the initial decay and subsequent rise of the 4-ring transition density. In the bottom panel, the decay of the 3-ring transition density for the group initially localized on the 3-ring segment is much more pronounced. In this case both possible pathways $S_3^{(3)} \rightarrow S_2^{(4)} \rightarrow S_1^{(4)}$ or $S_2^{(3)} \rightarrow S_1^{(4)}$ lead to energy transfer and can be mapped onto a two-state model.

These two groups can be further separated based on the initial excited state; either S_2 or S_3 can serve as the initial state. Here we focus on group (ii) initially localized on the 3-ring segment, giving rise to $\left\langle (\rho^{ga})_{3\text{-ring}}^2 \right\rangle_{N_{S_2^{(3)}}}$ and $\left\langle (\rho^{ga})_{3\text{-ring}}^2 \right\rangle_{N_{S_3^{(3)}}}$ where $N_{S_2^{(3)}}$ and $N_{S_3^{(3)}}$ are provided in Table 2. Next, let us continue to divide the 3-ring transition density decay from trajectories initially localized on the 3-ring segment into contributions from those initially promoted to $S_2^{(3)}$ and those promoted to $S_3^{(3)}$ shown in Fig. 7. Since the simulated laser pulse was chosen in order to maximize selection of the second excited state, it is no surprise that the main contribution arises from this group, shown in the top panel of Fig. 7. In fact, this group can hardly be distinguished from the previous 3-ring decay in the bottom panel of Fig. 6. However, a small subset of

the trajectories exhibiting initial transition density localized on the 3-ring segment are in the higher energy $S_3^{(3)}$ configuration. This group gives rise to a distinctly different transfer dynamics, shown in the bottom panel of Fig. 7.

The energy transfer occurs at a faster rate for trajectories initially promoted to $S_3^{(3)}$ than $S_2^{(3)}$. This is expected based on the relative energy differences for the two systems[29] shown in the histograms in Fig. 8. For the system initially in $S_2^{(3)}$, the relevant transition is $S_2^{(3)}$–$S_1^{(4)}$, and the corresponding energy gap $\Delta E_{12} = (E_2 - E_1)$ has an average value 0.12 eV and a standard deviation of 0.10 eV when the system is evolving on S_2. However, when the system is initially in $S_3^{(3)}$, the relevant transition is $S_3^{(3)}$–$S_2^{(4)}$. In this case, the corresponding energy gap $\Delta E_{23} = (E_3 - E_2)$ has an average value of 0.07 eV and a standard deviation of 0.05 eV when the system is evolving on S_3. The smaller energy gap and the narrower distribution for the relevant transition for $S_3^{(3)}$ leads to a faster energy transfer rate. The larger average value ΔE_{12} of 0.25 eV is irrelevant in this case, because it corresponds to the $S_2^{(4)}$–$S_1^{(4)}$ transition where energy transfer is not involved.

Finally, we have calculated rates for the 3-ring transition density decay for each component piece (total transition density, initial density on 3-rings $S^{(3)}$, initially promoted to $S_2^{(3)}$ or $S_3^{(3)}$). Only the 4 largest distances (50–500 Å) were included in the fit to
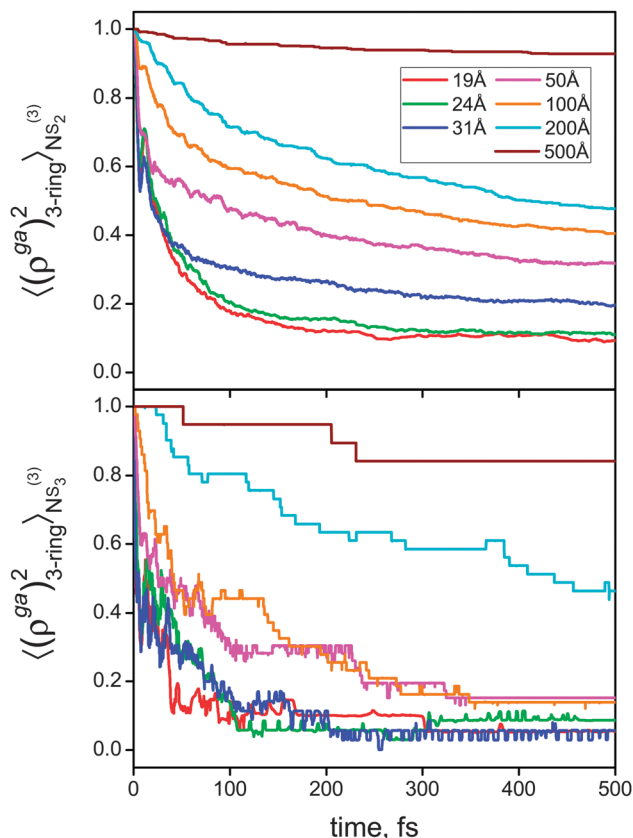

Fig. 7 The transition density for trajectories initially localized on the 3-ring segment is divided into contributions from (top) those initially promoted to $S_2^{(3)}$ and (bottom) those initially promoted to the higher energy $S_3^{(3)}$ state. The change in the electronic transition density with time is plotted for each separation distance.
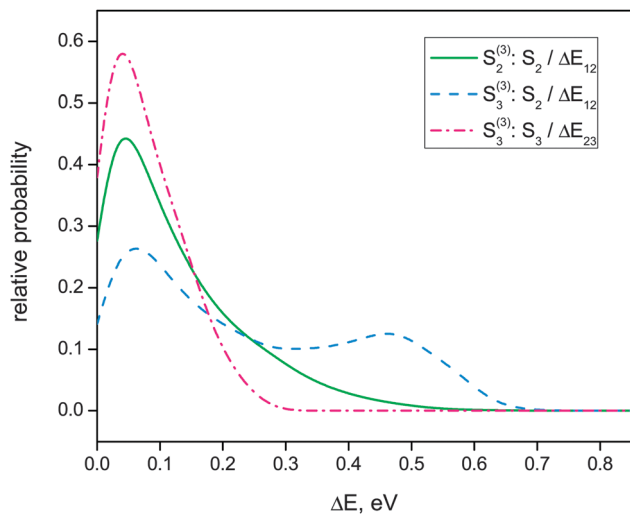
Fig. 8 Histograms of the energy gaps for the 50 Å system where the height of each point corresponds to the fraction of trajectories with the given energy gap. For trajectories initially promoted to $S_2^{(3)}$, the energy gap ΔE_{12} is plotted for all times when the system is evolving on S_2. For trajectories initially promoted to $S_3^{(3)}$, the energy gaps ΔE_{23} and ΔE_{12} are plotted for all times when the system is evolving on S_3 and S_2, respectively.
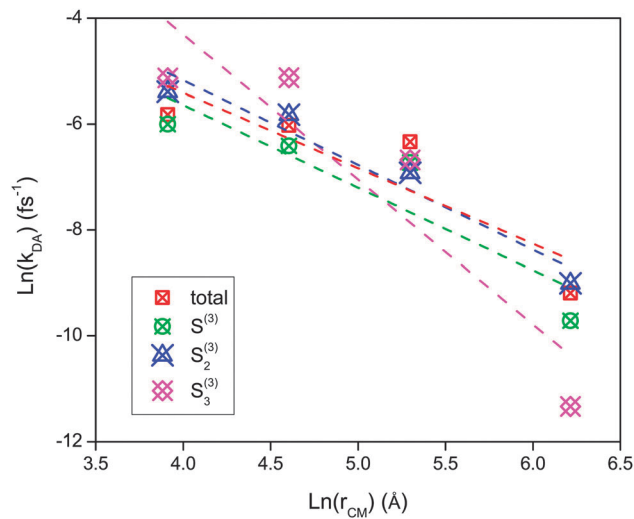

Fig. 9 Log–log plot of the transition density decay rate, k_{DA}, for each separation distance, r_{CM}, for the total density (red squares), the contribution from all trajectories initially localized on the 3-ring segment $S^{(3)}$ (green circles), and then separately for those initially promoted to $S_2^{(3)}$ (blue triangles) and $S_3^{(3)}$ (magenta diamonds). The data has been fit to a linear function (dashed lines) whose slope is related to the scaling provided in Table 3 along with the rates.

ensure that the point dipole approximation is valid. Fig. 9 shows a log–log plot of the calculated rates (k_{DA}) for each separation distance, r_{CM}, for all of the component pieces. In order to determine the scaling with r_{CM}, a linear fit ($f(x) = c - bx$) was performed, the fits are plotted as dashed lines. Here, the slope b is related to the power function scaling ($f(x) = ax^{-b}$). The rates can be found in Table 3 where the value of b is also provided to indicate the scaling. Fits were also performed using only the 3 largest distances (100–500 Å). The expected $1/r^6$ scaling for Förster type energy transfer is not achieved for any of the components, but we find that as we restrict the fit to larger separation distances, the scaling improves. At this point, we have not considered the role of torsional fluctuations in our analysis; the complex energy transfer is controlled by two mechanisms – electronic transitions and torsional fluctuations. We will discuss torsional fluctuations in the next section.

B. Effect of conformational disorder on relaxation pathways

So far, we have demonstrated that the initial configuration of PPV segments combined with their overlapping absorbance leads to multiple pathways for energy transfer. Conformational twisting during dynamics further complicates the picture by changing the relative energy ordering of the states depending on the instantaneous configuration. Sudden changes in the electronic transition density localization can occur due to conformational fluctuations. There are two torsion angles and both can effect excitation localization: rotation around the double bond relating to the *cis–trans* configuration, or rotation of the aromatic ring around its own axis. Since the *trans* configuration of distyrylbenzene is very stable, we do not observe large fluctuations in the rotation around the double bond during dynamics.[49] Therefore, we only consider the latter

rotation giving the relative angle between neighboring aromatic rings ranging from 0° for the co-planar arrangement to 90° for perpendicular alignment. Fluctuations can cause either a small increase or decrease in the dihedral angle between monomer PV subunits. As the dihedral angle increases, the polymer backbone develops a kink, and conjugation is broken. Changes in the transititon density localization are caused by the interaction between the different electronic excited states and reflects the degree to which electronic transitions between states takes place. Conformational fluctuations change the interaction between the states by modifying the coupling between them. This is certainly more pronounced for large dihedral angles where the polymer backbone develops a kink, and conjugation is broken.

It is reasonable to assume that trajectories initially in the $S_2^{(4)}$ or $S_3^{(3)}$ states are caused by configurational disorder and should exhibit large dihedral angles since they have an energy ordering that differs with respect to the planar geometry. Likewise it would be natural to predict that trajectories initially in the $S_2^{(3)}$ or $S_3^{(4)}$ states should exhibit small dihedral angles since they have an energy ordering consistent with the planar geometry. After dividing the trajectories according to their initial state ($S_2^{(4)}$, $S_3^{(3)}$, $S_2^{(3)}$, or $S_3^{(4)}$), we have constructed the histograms shown in Fig. 10 of the twist angles between each monomer PV subunit for the initial configurations of the system separated by $r_{CM} = 50$ Å. The height of the histograms corresponds to the fraction of trajectories with a given angle. Although trajectories initially in $S_2^{(4)}$ and $S_3^{(3)}$ do exhibit large dihedral angles as expected, these large angles are also prevalent in trajectories initially promoted to $S_2^{(3)}$ and $S_3^{(4)}$. While some of the twisted configurations cause reordering of the excited states, in other cases they give rise to the same energy ordering as the planar geometry. As a consequence, the presence of large dihedral

9252 | *Phys. Chem. Chem. Phys.*, 2013, **15**, 9245–9256

This journal is © the Owner Societies 2013

Table 3 Energy transfer rates (k_{DA}, fs^{-1}) for the decay of electronic transition densities

r_{CM} (Å)	Total	$S^{(3)}$	$S_2^{(3)}$	$S_3^{(3)}$
19	0.0016	0.0036	0.0033	0.0082
24	0.0020	0.0034	0.0035	0.019
31	0.0016	0.0026	0.0024	0.018
50	0.0030	0.0025	0.0023	0.0059
100	0.0024	0.0016	0.0015	0.0059
200	0.0018	0.0012	0.0012	0.0013
500	1.02×10^{-4}	6.05×10^{-05}	6.12×10^{-05}	1.19×10^{-05}
4-point scaling (b)	1.43	1.56	1.60	2.73
3-point scaling (b)	2.03	2.11	2.00	3.92

angles is not sufficient to predict which energy transfer pathway will occur. Instead, the relative placement of the angles and how they evolve in time must be considered.

Let us now consider a single trajectory from the system separated by r_{CM} = 50 Å demonstrating the 3-rings → 4-rings energy transfer via the $S_2^{(3)} \rightarrow S_1^{(4)}$ pathway which occurs within the first 50 fs of the dynamics. The potential energy for the lowest two excited states is shown in the top panel of Fig. 11 where the blue state is localized on the 4-ring segment and the red state is localized on the 3-ring segment. The dashed line shows the path followed during the dynamics. The evolution of the electronic transition density is shown in the middle panel of Fig. 11 for each segment as well as the contributions from each monomer subunit (see Fig. 1), and the dihedral angles are shown in the bottom panel.

The system is initially promoted to $S_2^{(3)}$ and the transition density is localized on the 3-ring segment. After 5 fs, a state crossing occurs, so that now the state localized on the 3-ring segment has lower energy ($S_2^{(3)} \rightarrow S_1^{(3)}$ and $S_1^{(4)} \rightarrow S_2^{(4)}$). During this time, energy transfer becomes unlikely since it requires transition to the much higher energy state localized on the 4-ring side. Possible energy transfer is postponed until the original energy ordering is restored when the states cross again at t = 16 fs. Since we have implemented the cross-detection algorithm, we are able to follow the diabatic state through the crossing points without causing sudden unphysical changes to the transition density (notice that the corresponding transition density remains localized on the 3-ring segment throughout the crossing regions). An electronic transition from $S_2^{(3)} \rightarrow S_1^{(4)}$ occurs at t = 22 fs where the system is in a region of strong coupling and the corresponding transition density moves to the 4-ring segment. At t = 40 fs, the states become nearly degenerate (without actually crossing) and the coupling is very strong, leading to the formation of a mixed state with density on both segments. Finally, the states separate in energy and the system continues to evolve on $S_1^{(4)}$.

The localization as well as the twisted instantaneous configurations are clearly visible in snapshots taken during dynamics provided in Fig. S1 of the ESI.† The state crossings in the previous example are caused by the changing twist angles between the monomer subunits (see bottom panel of Fig. 11, Fig. S1, ESI†). Although the excitation is initially localized on the 3-ring segment, the initial configuration is twisted. The large $\alpha 1$ and $\beta 3$ angles disrupt the backbone conjugation resulting in an effective 2-ring sub-fragment on the 3-ring side, and a 3-ring sub-fragment on the 4-ring side. Notice that at t = 0 fs, the density primarily localizes on the 2-ring sub-fragment composed of $a2$ and $a3$ (middle panel of Fig. 11). Subtle fluctuations in the angles near the critical values lead to the state crossings and near degeneracy. As $\beta 1$ becomes larger, the 3-ring sub-fragment on the 4-ring side is reduced to 2-rings, leaving a system of two 2-ring sub-fragments on either segment, and the energy ordering becomes highly sensitive to small fluctuations in the angles. On the 4-ring side, the density is primarily localized to the middle two rings, $b2$ and $b3$. As $\alpha 2$ becomes larger, the state localized on the 3-ring side remains at higher energy.

We now turn our attention to another example of 3-rings → 4-rings energy transfer where the pathway involved is $S_3^{(3)} \rightarrow S_1^{(4)}$. The energy of the trajectory is shown in the top panel of Fig. 11 as a dashed line and the energies of the three lowest excited states are also shown where blue states are localized on the 4-ring segment and the red state is localized on the 3-ring segment. Again, there is a trivial unavoided crossing within the first 10 fs where the energy of the state localized on the 3-ring
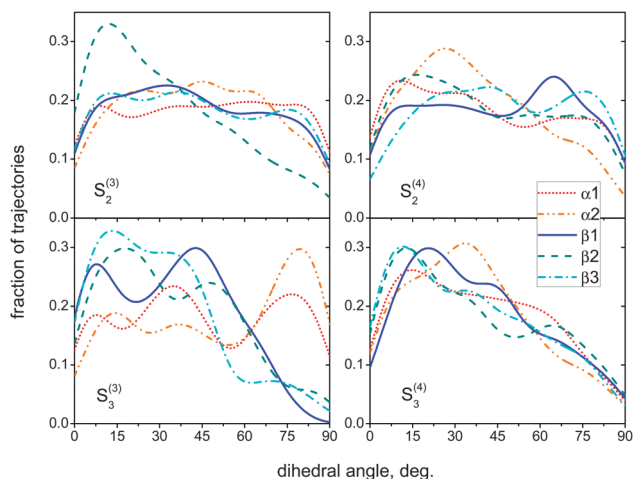

Fig. 10 Histograms of the dihedral angles between monomer PV subunits for each initial configuration for the 50 Å systems. The height of the histograms corresponds to the fraction of trajectories with a given angle. Color coding corresponds to the angles labeled in Fig. 1. Large dihedral angles are present in all cases regardless of the initial state or transition density localization. Some twisted configurations alter the energy ordering while in other cases the energy ordering is preserved despite the presence of large angles.
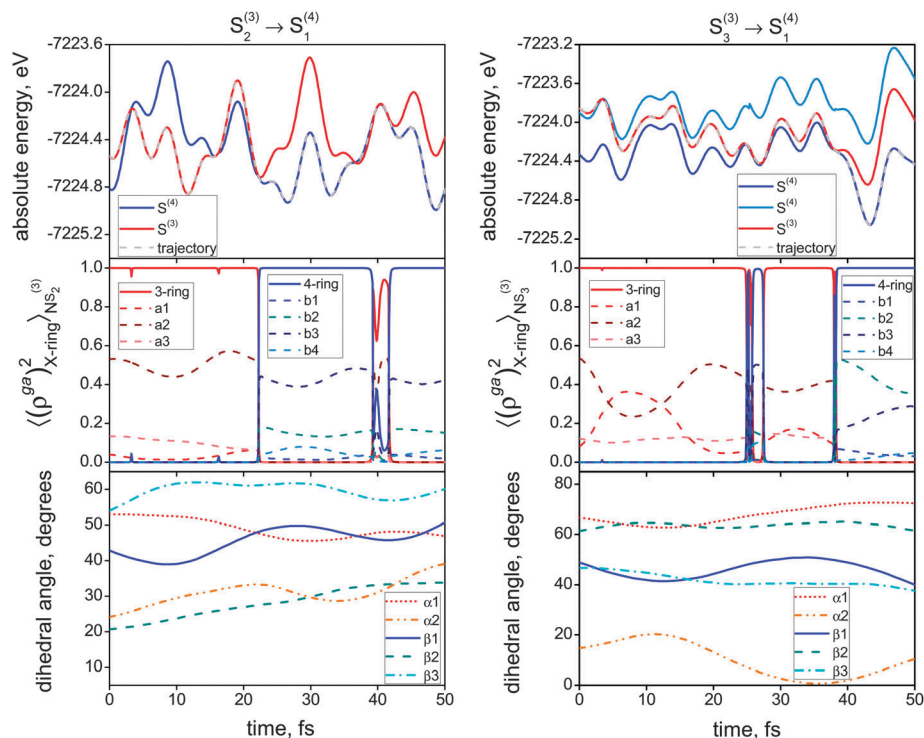
This journal is © the Owner Societies 2013

Phys. Chem. Chem. Phys., 2013, **15**, 9245–9256 | **9253**

Fig. 11 Single trajectories representing the $S_2^{(3)} \rightarrow S_1^{(4)}$ and $S_3^{(3)} \rightarrow S_1^{(4)}$ pathways. Top: The potential energy of the lowest energy excited states where blue states are localized on the 4-ring segment the and red state is localized on the 3-ring segment. The energy pathway followed by the trajectory is shown by the dashed line. Middle: Transition density of the 3-rings and 4-ring segments. Bottom: evolution of the dihedral angles for the angles between each monomer PV subunit.

side falls to lower energy ($S_3^{(3)} \rightarrow S_2^{(3)}$ and $S_2^{(4)} \rightarrow S_3^{(4)}$). The system initially in $S_3^{(3)}$ follows the 3-ring state through the cross and remains on $S_2^{(3)}$ until a region of strong coupling at $t = 25$ fs where it transitions to $S_1^{(4)}$ for a few fs before returning to $S_2^{(3)}$. Finally, at $t = 39$ fs, the system hops to $S_1^{(4)}$ and the transition density is transferred to the 4-ring side. In this example, the reordering of excited state energies does not delay the energy transfer, since the $S_1^{(4)}$ state is not involved in the crossings and remains consistently at lower energy.

The middle and bottom panels in Fig. 11 provide some insight into the role of configuration, and corresponds to the snapshots taken along the trajectory shown in Fig. S2 of ESI.† The initial localization favors the $a2$ subunit because of the large angle at site $\alpha 1$. A slight decrease in the $\alpha 1$ angle by $t = 10$ fs causes the density on the $a1$ subunit to substantially increase before falling as $\alpha 1$ rises again. At $t = 25$ fs, $S_1^{(4)}$ and $S_2^{(3)}$ become nearly degenerate and the system hops to $S_1^{(4)}$. The system passes through a mixed state at the moment of hopping. The system hops back to $S_2^{(3)}$ before leaving the region of strong coupling and the final transition to $S_1^{(4)}$ occurs $t = 39$ fs where the large angles at $\beta 1$ and $\beta 2$ keep the density primarily localized to $b2$ and $b3$ sub-fragments.

Static disorder in the ensemble leads to the formation of configurational sub-fragments of varying lengths, which localizes the initial excitation in different segments of chromophores and leads to multiple pathways for energy transfer. On the other hand, the role of dynamic disorder is more difficult to predict. This leads to complex energy transfer processes. In the

first example shown in this section, the state localized on the 3-ring side, has initially high energy. Dynamical excited state energy reordering due to conformational fluctuations brings the state to lower energy leading to a delay in energy transfer. In the second example, such reordering brings the state localized on the 3-ring side to lower energy, but the $S_1^{(4)}$ state remains unaffected. Therefore, the system is not prevented from making the transition to the 4-ring side (due to energy constraints). However, as we demonstrated in the previous section, the relative energy gap is affected by the state cross ($\Delta E_{23} < \Delta E_{12}$), and thus the rate changes substantially.

IV. Conclusion

We have used non-adiabatic excited state molecular dynamics to model the energy transfer in a system composed of weakly coupled 3-ring and 4-ring PPV segments separated by varying distances. In conjugated polymer systems, the initial excitation can be localized in either segment because of the overlapping absorption of the fragments. This gives rise to multiple energy transfer pathways which occur simultaneously including 3-ring → 4-rings and the reverse 4-rings → 3-rings transfer. It is also possible for the system to remain localized on the same segment throughout the electronic relaxation process.

The $1/r^6$ scaling for energy transfer rates predicted by the Förster model was not followed for this system. However, the scaling was improved by analyzing the various pathways separately depending on the localization of the initial excitation

and considering only the largest separation distances. Configurational disorder caused by large dihedral angles between monomer PV subunits adds yet another layer of complexity. Kinks in the backbone of the polymer break the conjugation and might or might not result in reordering of the excited state energy levels. As we have shown, the presence of large dihedral angles is not sufficient criterion to determine what pathway is involved. We suspect that it should be possible to recover the Förster scaling for these polymer systems by further treating each of the configurations separately. However, given the large number of possible configurations in these systems, the number of NA-ESMD trajectories required to achieve statistical convergence quickly becomes very large even for the smallest systems. Also, the configuration can change during the course of the dynamics due to small fluctuations in the twist angles.

In general, energy transfer proceeds at a faster rate when the system is initially promoted to S_3 compared to beginning in S_2. The energy gap separating S_3 and S_2 is, in most cases, smaller than the gap separating S_2 and S_1. Stronger electronic coupling promotes fast S_3–S_2 relaxation. An exception is the case following the $S_3^{(4)} \rightarrow S_2^{(4)} \rightarrow S_1^{(3)}$ pathway where the gap between S_2 and S_1 must be overcome before energy transfer occurs. Therefore, the rate of energy transfer depends on the initial state, energy gaps, and the specific ordering of the excited states. As we have seen from our analysis, subtle fluctuations in the twist angles between monomer subunits can lead to multiple state crossings throughout the dynamics. Therefore, the results here will be very sensitive to parameters chosen for the cross-detection algorithm. If the unavoided crosses are not detected properly, the result will be a very fast back-and-forth energy transfer as the system follows the adiabatic state, whose identity and localization are changing in time.

It should be noted that within the FSSH approach, electronic subsystem in every independent trajectory undergoes fully coherent evolution. That is, phase information is retained at all times and electronic states are more coherent than they otherwise should be. Since vibrational degrees of freedom/bath are treated classically, there are no dissipative mechanisms for electronic coherences. Interactions between conjugated segments favor delocalized states. For the times in which there is a well-defined phase relationship between segments, coherent energy transfer mechanisms exist. Interactions with molecular nuclear motions or the solvent environment destroy phase coherence and cause localized excitations to be stabilized. In the case of dephased segments, energy transfer can then occur randomly in a stochastic fashion (described as a hopping mechanism or weak interaction limit). In conjugated polymers and dendrimers, both mechanisms can make significant contributions to the dynamics of energy transfer.[69] These factors cause our simulated energy transfer rates to be faster than those reported from polarization anisotropy decay measurements for MEH-PPV.[31,47,48]

In conclusion, Förster theory must be applied very carefully (if at all) in modeling energy transfer in conjugated polymer systems such as PPV. The energy transfer in these systems cannot be described by a single well-defined pathway due to the configurational disorder where multiple excitations and chromophores are involved, and where the absorbance of donor and acceptor are not well separated. Even for the smallest systems, the number of configurations that must be considered grows very quickly. In addition, excitations can be delocalized over electronically coupled donor and acceptor chromophores at short separation distances. The added complexity of the dynamical configurational disorder leads to excited state energy reordering and complex rates that are not suited for a typical Förster model based on single rate description.

Acknowledgements

References

1 G. Malliaras and R. Friend, *Phys. Today*, 2005, **58**, 53–58.
2 S. Gunes, H. Neugebauer and N. Sariciftci, *Chem. Rev.*, 2007, **107**, 1324–1338.
3 A. J. Heeger, *Chem. Soc. Rev.*, 2010, **39**, 2354–2371.
4 J. L. Bredas, J. E. Norton, J. Cornil and V. Coropceanu, *Acc. Chem. Res.*, 2009, **42**, 1691–1699.
5 D. G. Kuroda, C. P. Singh, Z. Peng and V. D. Kleiman, *Science*, 2009, **326**, 263–267.
6 J. Clark and G. Lanzani, *Nat. Photonics*, 2010, **4**, 438–446.
7 C. McNeill and N. Greenham, *Adv. Mater.*, 2009, **21**, 3840–3850.
8 M. A. Baldo, M. E. Thompson and S. R. Forrest, *Nature*, 2000, **403**, 750–753.
9 B. Schwartz, *Annu. Rev. Phys. Chem.*, 2003, **54**, 141–172.
10 P. F. Barbara, W. S. Chang, S. Link, G. D. Scholes and A. Yethiraj, *Annu. Rev. Phys. Chem.*, 2007, **58**, 565–584.
11 V. K. Thorsmolle, R. D. Averitt, J. Demsar, D. L. Smith, S. Tretiak, R. L. Martin, X. Chi, B. K. Crone, A. P. Ramirez and A. J. Taylor, *Phys. Rev. Lett.*, 2009, **102**, 017401.
12 H. Tamura, E. R. Bittner and I. Burghardt, *J. Chem. Phys.*, 2007, **126**, 021103.
13 G. D. Scholes and G. Rumbles, *Nat. Mater.*, 2006, **5**, 683–696.
14 F. C. Spano, *Annu. Rev. Phys. Chem.*, 2006, **57**, 217–243.
15 T. Forster, *Ann. Phys.*, 1948, **437**, 55.
16 B. P. Krueger, G. D. Scholes and G. R. Fleming, *J. Phys. Chem. B*, 1998, **102**, 5378–5386.
17 W. Ortiz, B. P. Krueger, V. D. Kleiman, J. L. Krause and A. E. Roitberg, *J. Phys. Chem. B*, 2005, **109**, 11512–11519.
18 S. Tretiak, C. Middleton, V. Chernyak and S. Mukamel, *J. Phys. Chem. B*, 2000, **104**, 9540–9553.

19 X. Michalet, S. Weiss and M. Jager, *Chem. Rev.*, 2006, **106**, 1785–1813.

20 P. Selvin, *Nat. Struct. Biol.*, 2000, **7**, 730–734.

21 J. Lakowicz, *Principles of Fluorescence Spectroscopy*, Springer Verlag, 2006.

22 K. P. Ghiggino, E. K. L. Yeow, D. J. Haines, G. D. Scholes and T. A. Smith, *J. Photochem. Photobiol., A*, 1996, **102**, 81–86.

23 W. Ortiz, A. E. Roitberg and J. L. Krause, *J. Phys. Chem. B*, 2004, **108**, 8218–8225.

24 F. Kleima, E. Hofmann, B. Gobets, I. van Stokkum and R. van Grondelle, *Biophys. J.*, 2000, **78**, 344–353.

25 A. Young and H. Frank, *J. Photochem. Photobiol., B*, 1996, **36**, 3–15.

26 T. Pullerits, S. Hess, J. Herek and V. Sundström, *J. Phys. Chem. B*, 1997, **101**, 10560–10567.

27 V. Sundström, T. Pullerits and R. van Grondelle, *J. Phys. Chem. B*, 1999, **103**, 2327–2346.

28 S. Fernandez-Alberti, A. Roitberg, V. Kleiman, T. Nelson and S. Tretiak, *J. Chem. Phys.*, 2012, **137**, 22A526.

29 S. Fernandez-Alberti, V. D. Kleiman, S. Tretiak and A. E. Roitberg, *J. Phys. Chem. Lett.*, 2010, **1**, 2699–2704.

30 J. Bolinger, M. Traub, J. Brazard, T. Adachi, P. Barbara and D. V. Bout, *Acc. Chem. Res.*, 2012, **45**, 1992–2001.

31 T. Dykstra, E. Hennebicq, D. Beljonne, J. Gierschner, G. Claudio, E. Bittner, J. Knoester and G. Scholes, *J. Phys. Chem. B*, 2009, **113**, 656–667.

32 B. V. Averbeke and D. Beljonne, *J. Phys. Chem. A*, 2009, **113**, 2677–2682.

33 K. Becker, E. D. Como, J. Feldmann, F. Scheliga, E. T. Csanyi, S. Tretiak and J. M. Lupton, *J. Phys. Chem. B*, 2008, **112**, 4859–4864.

34 S. Tretiak, A. Saxena, R. L. Martin and A. R. Bishop, *Phys. Rev. Lett.*, 2002, **89**, 097402.

35 J. Clark, T. Nelson, S. Tretiak, G. Cirmi and G. Lanzani, *Nat. Phys.*, 2012, **8**, 225–231.

36 E. Collini and G. Scholes, *Science*, 2009, **323**, 369–373.

37 S. Jang and Y.-C. Cheng, *Wiley Interdisc. Rev.: Comput. Mol. Sci.*, 2013, **3**, 84–104.

38 S. Jang, M. D. Newton and R. J. Silbey, *Phys. Rev. Lett.*, 2004, **92**, 218301.

39 G. D. Scholes, *Annu. Rev. Phys. Chem.*, 2003, **54**, 57–87.

40 G. D. Scholes and G. R. Fleming, *J. Phys. Chem. B*, 2000, **104**, 1854–1868.

41 H. Sumi, *J. Phys. Chem. B*, 1999, **103**, 252–260.

42 K. Mukai, S. Abe and H. Sumi, *J. Phys. Chem. B*, 1999, **103**, 6096–6102.

43 P. Yang, E. R. Batista, S. Tretiak, A. Saxena, R. L. Martin and D. L. Smith, *Phys. Rev. B: Condens. Matter Mater. Phys.*, 2007, **76**, 241201.

44 S. Kilina, E. R. Batista, P. Yang, S. Tretiak, A. Saxena, R. L. Martin and D. L. Smith, *ACS Nano*, 2008, **2**, 1381–1388.

45 V. Lukes, R. Solc, M. Barbatti, H. Lischka and H.-F. Kauffmann, *J. Theor. Comput. Chem.*, 2010, **9**, 249–263.

46 S. Karabunarliev, E. R. Bittner and M. Baumgarten, *J. Chem. Phys.*, 2001, **114**, 5863–5870.

47 M. M.-L. Grage, P. W. Wood, A. Ruseckas, T. Pullerits, W. Mitchell, P. L. Burn, I. D. W. Samuel and V. Sundstrom, *J. Chem. Phys.*, 2003, **118**, 7644.

48 K. M. Gaab and C. J. Bardeen, *J. Phys. Chem. B*, 2004, **108**, 4619–4626.

49 T. Nelson, S. Fernandez-Alberti, V. Chernyak, A. E. Roitberg and S. Tretiak, *J. Phys. Chem. B*, 2011, **115**, 5402–5414.

50 S. Fernandez-Alberti, A. Roitberg, T. Nelson and S. Tretiak, *J. Chem. Phys.*, 2012, **137**, 014512.

51 S. Tretiak, C. Isborn, A. Niklasson and M. Challacombe, *J. Chem. Phys.*, 2009, **130**, 054111.

52 F. Furche and R. Ahlrichs, *J. Chem. Phys.*, 2002, **117**, 7433–7447.

53 R. Send and F. Furche, *J. Chem. Phys.*, 2010, **132**, 044107.

54 S. Tretiak and S. Mukamel, *Chem. Rev.*, 2002, **102**, 3171–3212.

55 S. Mukamel, S. Tretiak, T. Wagersreiter and V. Chernyak, *Science*, 1997, **277**, 781–787.

56 M. J. S. Dewar, E. G. Zoebisch, E. F. Healy and J. J. P. Stewart, *J. Am. Chem. Soc.*, 1985, **107**, 3902–3909.

57 K. Drukker, *J. Comput. Phys.*, 1999, **153**, 225–272.

58 J. Tully, *J. Chem. Phys.*, 1990, **93**, 1061–1071.

59 J. C. Tully, *J. Chem. Phys.*, 2012, **137**, 22A301.

60 L. Verlet, *Phys. Rev.*, 1967, **159**, 98–103.

61 M. P. Allen and D. J. Tildesley, *Computer Simulation of Liquids*, Clarendon Press, Oxford, 1987.

62 M. Paterlini and D. Ferguson, *Chem. Phys.*, 1998, **236**, 243–252.

63 T. Nelson, S. Fernandez-Alberti, V. Chernyak, A. Roitberg and S. Tretiak, *J. Chem. Phys.*, 2012, **136**, 054108.

64 F. Plasser and H. Lischka, *J. Chem. Theor. Comput.*, 2012, **8**, 2777–2789.

65 S. Tretiak and V. Chernyak, *J. Chem. Phys.*, 2003, **119**, 8809–8823.

66 B. P. Krueger, G. D. Scholes, R. Jimenez and G. R. Fleming, *J. Phys. Chem. B*, 1998, **102**, 2284–2292.

67 A. Olaya-Castro and G. D. Scholes, *Int. Rev. Phys. Chem.*, 2011, **30**, 49–77.

68 W. J. D. Beenken and T. Pullerits, *J. Chem. Phys.*, 2004, **120**, 2490.

69 O. Varnavski, J. Ostrowski, L. Sukhomlinova, R. Twieg, G. Bazan and T. Goodson, *J. Am. Chem. Soc.*, 2002, **124**, 1736–1743.